Sawtooth Mass Dependence of Fission-Fragment Angular Momenta in the Spontaneous Fission of ^{252}Cf

A. Rahmatinejad[1†] N. Ryzhkov[1] T. M. Shneidman[1] G. G. Adamian[1] N. V. Antonenko[1,2]

[1]Joint Institute for Nuclear Research, Dubna, 141980, Russia
[2]Tomsk Polytechnic University, Tomsk, 634050, Russia

Abstract: The mass dependence of fission-fragment angular momenta is investigated for the spontaneous fission of ^{252}Cf within the dinuclear-system (DNS) model. After penetrating the fission barrier, the system evolves through an ensemble of touching fragment configurations in mass, charge, and deformation space, while the collective angular motion is treated quantum mechanically. The calculated fragment angular momenta closely reproduce the experimentally observed mass-dependent trends and the pronounced minimum near $A \simeq 132$. The sawtooth structure persists after averaging over all charge partitions contributing to a given fragment mass, demonstrating that it is a robust property of the scission ensemble rather than a consequence of the particular isotope sequence selected experimentally. The results highlight the central role of shell-dependent fragment deformation in the generation of fission-fragment angular momentum. The same scission ensemble also reproduces the observed anticorrelation between the total kinetic energy (TKE) and the total prompt-neutron multiplicity, providing further support for the calculated scission configurations.

Keywords: spontaneous fission, angular momentum of fission fragments, scission point model

DOI: 10.1088/1674-1137/aeba7a **CSTR:**

CPC Accepted

I. INTRODUCTION

Nuclear fission produces a rich set of correlated fragment observables that reflect the dynamics of the system near scission. During fission, the available energy and angular momentum are distributed among different degrees of freedom, including the relative motion of the fragments and their intrinsic and collective excitations. Fragment mass and charge yields, total kinetic energy (TKE), prompt-neutron emission, and fragment angular momenta therefore provide complementary information about the properties of the fissioning system and its configuration near scission. A consistent description of the correlations among these observables provides a particularly demanding test of a fission model because it probes both the relative populations of the various fragment configurations at scission and their excitation energies and collective dynamics.

The average number of prompt neutrons emitted by a fragment exhibits the well-known sawtooth dependence on fragment mass [1, 2]. In ^{252}Cf spontaneous fission, the neutron multiplicity varies strongly across the fragment-mass distribution, with a pronounced minimum near the heavy-fragment shell region. Prompt-neutron emission is also strongly correlated with the total kinetic energy of the fragments: higher-TKE events are associated, on average, with lower neutron multiplicities [1, 2]. These systematic dependences provide complementary constraints on the excitation of the primary fragments. Neutron multiplicity and TKE are closely connected to the fragment configurations at scission and, in particular, to their deformations, which influence both the kinetic energy of the separating fragments and the excitation generated by subsequent shape relaxation [3−5]. Fragment deformations at scission also play an important role in determining the angular-momentum distributions of the emerging fragments through the deformation-dependent interaction and the associated collective angular motion [6].

Recent measurements have revealed a pronounced mass dependence of fission-fragment angular momentum [7]. The average angular momentum displays a sawtooth-like structure, including strong suppression near $A \simeq 132$. The dependence of fragment angular momentum on TKE provides a complementary experimental constraint. For ^{144}Ba produced in the spontaneous fission of ^{252}Cf, only a weak variation of the average angular momentum with TKE was observed [8], a behavior subsequently described within the DNS approach [9]. The angular momenta of complementary fragments were found to be only weakly correlated, while the angular momentum of a

Received 30 August 2026; Accepted 28 October 2026

† E-mail: a_rahmatinejad@theor.jinr.ru

©2027 Chinese Physical Society and the Institute of High Energy Physics of the Chinese Academy of Sciences and the Institute of Modern Physics of the Chinese Academy of Sciences and IOP Publishing Ltd. All rights, including for text and data mining, AI training, and similar technologies, are reserved.

given fragment showed little dependence on the identity of its partner. Taken together, these observations provide a detailed experimental picture against which mechanisms of angular-momentum generation in fission can be tested.

Several mechanisms have been proposed to explain the generation and mass dependence of fission-fragment angular momenta. Wilson et al. [7] interpreted the weak correlations between the angular momenta of complementary fragments in terms of independent torques associated with neck rupture. Statistical descriptions instead populate the bending, wriggling, twisting, and tilting modes according to their effective temperatures and moments of inertia [10, 11]. In these approaches, the spin magnitudes are governed by excitation energy, shell structure, and angular-momentum-dependent level densities. A related dynamical approach couples Langevin shape evolution to nucleon-exchange transport and finds that the rotational modes can fall out of equilibrium before scission as the neck disappears [12].

Microscopic symmetry-restoration and angular-momentum-projection calculations provide a complementary perspective [13−16]. These calculations extract fragment-spin distributions directly from many-body states and show that the intrinsic fragment spins and their relative orbital angular momentum are constrained by fission dynamics and total angular-momentum conservation. A recent extension of the projection and time-dependent-configuration-mixing framework to the full range of fragment masses reproduces a pronounced sawtooth dependence and finds a strong correlation between spin and scission deformation, but only a weak correlation between the magnitudes of complementary-fragment spins [17, 18].

Collective Hamiltonian calculations provide another description of angular-momentum generation, in which quantum angular fluctuations and the orientation-dependent interaction between deformed fragments can generate substantial fragment angular momenta [19]. The role of such angular fluctuations at scission was studied in detail in Ref. [6], where the collective angular motion of two touching fragments was treated quantum mechanically. Within this picture, the interaction has a local minimum at the axially symmetric pole-to-pole configuration and tends to localize the fragment symmetry axes around this configuration. The collective angular motion explores configurations displaced from this minimum and therefore dynamically breaks axial symmetry, while the equilibrium configuration itself remains axially symmetric. The resulting localization of the angular coordinates necessarily implies, through the angle–angular-momentum uncertainty relation, a finite spread in the fragment angular momenta. Angular fluctuations at scission may therefore provide a general quantum-mechanical mechanism for generating fragment angular momentum. This mechanism has recently been investigated within a microscopic framework, in which a substantial part of the projected fragment-spin distribution was likewise related to the uncertainty between fragment orientation and angular momentum, with quadrupole deformation providing the dominant contribution [20]. Recent time-dependent microscopic calculations also show that intrinsic nonaxial shape degrees of freedom can modify fission-fragment spin distributions and correlations [21].

In the present work, we employ the dinuclear-system (DNS) model developed in our previous studies [6, 9, 22]. After tunneling through the fission barrier, the system is described as an ensemble of interacting fragment configurations whose evolution toward scission is governed by a master equation. The angular vibrations of the fragments are treated quantum mechanically and are largely determined by their deformations at scission. After scission, the relaxation of the fragments from their nonequilibrium shapes converts deformation energy into intrinsic excitation. This excitation is subsequently released through the prompt-neutron evaporation cascade, which determines the neutron multiplicity and transforms the primary-fragment properties into the corresponding post-neutron fragment observables. This framework has previously been applied to describe the main fission observables, including fragment yields, TKE, neutron emission, and angular-momentum characteristics. In the present calculations, we use the same set of model parameters as in our previous studies and focus on the mass dependence of the fragment angular momenta and its relation to the scission configurations.

The paper is organized as follows. Section II summarizes the DNS evolution, the calculation of TKE and fragment excitation energies, the quantum-mechanical treatment of angular motion, and the conversion from primary to post-neutron fragment observables. The calculated deformation distributions, the mass dependence of fragment angular momentum, and the neutron–TKE correlation are discussed in Sec. III. The main conclusions are summarized in Sec. IV.

II. MODEL

After tunneling through the fission barrier, the fissioning nucleus is described as an ensemble of DNS configurations, each consisting of two interacting fragments in contact. A DNS configuration, denoted by q, is specified by the fragment masses $A_{1,2}(q)$, charges $Z_{1,2}(q)$, and deformations $\beta_{1,2}(q)$. For each configuration, mass and charge conservation require $A_1(q)+A_2(q)=A_{\rm CN}$ and $Z_1(q)+Z_2(q)=Z_{\rm CN}$, where $A_{\rm CN}=252$ and $Z_{\rm CN}=98$ are the mass and charge numbers of the fissioning nucleus.

The angular motion of the DNS generates the fragment angular momenta (see Ref. [6]), whereas motion along the relative-distance coordinate R governs the sep-

CPC Accepted

aration of the DNS into primary fission fragments. The description of the collective evolution of the DNS toward scission and the quantum-mechanical treatment of its angular motion follow Refs. [6, 9, 22]. Below, we summarize the principal elements of the model and introduce the quantities required to calculate the mass-dependent average fragment angular momentum, its post-neutron counterpart, and the neutron–TKE correlation.

A. Evolution of the dinuclear system

The collective evolution is formulated in a discrete DNS configuration space spanned by the fragment mass and charge partitions and the deformations of the two fragments. Each point in this space is labeled by $q = \{A_1, Z_1, \beta_1, \beta_2\}$, where A_1 and Z_1 are the mass and charge numbers of one fragment, and β_1 and β_2 characterize the deformations of the two complementary fragments. The relative-distance coordinate R and the angular degrees of freedom are not included in q and are treated separately.

For a given DNS configuration, the potential energy as a function of the internuclear distance is expressed as

$$U(q,R) = B_1(q) + B_2(q) - B_{\rm CN} + V_{\rm int}(q,R), \tag{1}$$

where B_1 and B_2 are the binding energies of the fragments, $B_{\rm CN}$ is the binding energy of the fissioning nucleus, and $V_{\rm int}$ includes the nuclear and Coulomb interactions between the fragments. For each configuration q, the fragments are assumed to be localized near the minimum $R_m(q)$ of the potential pocket in the relative-distance coordinate, with the fragments in a pole-to-pole orientation. The potential-energy surface governing the evolution in fragment mass, charge, and deformation space is obtained by evaluating the DNS potential at this minimum, $U(q) = U(q, R_m(q))$.

In the present model, the DNS configuration evaluated at $R_m(q)$ is identified with the scission configuration. The fragment masses, charges, deformations, excitation energies, and angular states at scission are therefore determined at this distance. The TKE assigned to this configuration includes both the interaction energy and the kinetic energy of relative motion at $R_m(q)$. Since the latter is not calculated explicitly, it is estimated from the minimum energy required to overcome the outer radial barrier at $R_b(q)$, as described in Sec. II B.

The system can evolve between neighboring DNS configurations through nucleon transfer and changes in fragment deformation. Concurrently, it can escape from the potential pocket in the relative-distance coordinate and separate into primary fission fragments. Thus, fission is treated as the decay of the DNS in the relative-distance coordinate R, in competition with its evolution in the fragment mass, charge, and deformation degrees of freedom.

The ensemble of DNS configurations populated immediately after tunneling through the fission barrier provides the initial condition for this evolution. Its probability distribution is denoted by $P_0(q) = P(q,0)$. The configurations contributing to $P_0(q)$ and their relative weights are specified in Sec. III A.

The time-dependent probability $P(q,t)$ of finding the system in configuration q is determined by the master equation

$$\frac{{\rm d}P(q,t)}{{\rm d}t} = \sum_{q'} \left[\lambda_{q'\to q} P(q',t) - \lambda_{q\to q'} P(q,t)\right] - \lambda_R(q) P(q,t), \tag{2}$$

where the sum runs over the configurations q' connected to q by nucleon transfer or a change in fragment deformation. The transition rate from q to q' is expressed as

$$\lambda_{q\to q'} = \kappa_{qq'}\, \rho\left[E^*(q'), q'\right], \tag{3}$$

where $\rho[E^*(q'), q']$ is the microscopic level density of the final DNS configuration. The microscopic transition probabilities are assumed to be symmetric and are parametrized as follows:

$$\kappa_{q'q} = \kappa_{qq'} = \frac{\lambda^{(j)}}{\sqrt{\rho\left[E^*(q), q\right]\rho\left[E^*(q'), q'\right]}}, \qquad j = A, \beta. \tag{4}$$

Here, $\lambda^{(A)}$ and $\lambda^{(\beta)}$ are model parameters for transitions associated with nucleon transfer and changes in fragment deformation, respectively [22].

The last term in Eq. (2) describes the loss of probability due to escape from the DNS potential pocket along the relative-distance coordinate. The corresponding decay rate is

$$\lambda_R(q) = \lambda^{(d)}(q)\, \rho_B\left[E^*(q) - V_B(q), q\right], \tag{5}$$

where $V_B(q) = U(q, R_b(q)) - U(q, R_m(q))$ is the barrier height along the relative-distance coordinate, and ρ_B is the DNS level density at the top of this barrier. When tunneling through the radial barrier is neglected, the microscopic decay probability is expressed as

$$\lambda^{(d)}(q) = \begin{cases} \dfrac{1}{\rho\left[E^*(q), q\right]}, & E^*(q) > V_B(q), \\ 0, & E^*(q) \le V_B(q). \end{cases} \tag{6}$$

If the radial potential has no outer barrier, $V_B(q) = 0$ and ρ_B is evaluated at the touching configuration [22].

The angular degrees of freedom are treated separ-

CPC Accepted

ately for each configuration q. Their eigenstates and eigenenergies are denoted by $\Psi_x^{\rm ang}(q)$ and $E_x^{\rm ang}(q)$, respectively, where x labels the angular-vibrational state. The index x is not included in the definition of q because the master equation describes evolution in the space of fragment masses, charges, and deformations. No phenomenological collective enhancement of the level density associated with angular motion is introduced, since these collective states are treated explicitly.

Because the characteristic temperatures in spontaneous fission are relatively low, the lowest angular-vibrational state is expected to provide the dominant contribution. This treatment does not assume that angular motion equilibrates faster than the DNS variables evolve. Rather, excited angular-vibrational states are energetically suppressed in the populated configurations, so the angular degree of freedom is dominated by its lowest state. When excited angular states become energetically accessible, their contributions can be included through the occupation probabilities.

$$w_x(q) = \frac{\rho_{\rm in}\left[E^*(q) - E_x^{\rm ang}(q), q\right]}{\sum_{x'}\rho_{\rm in}\left[E^*(q) - E_{x'}^{\rm ang}(q), q\right]}, \tag{7}$$

where $\rho_{\rm in}$ is the intrinsic level density. In the low-temperature limit, this expression reduces to the approximation $w_x(q) \simeq \delta_{x0}$. Occupation of the angular ground state does not imply vanishing fragment angular momenta because this state is a superposition of different coupled fragment-angular-momentum components.

The probability of producing the primary-fragment configuration q is obtained by integrating the probability flux associated with decay along the relative-distance coordinate:

$$P_f(q) = \int_0^\infty \lambda_R(q) P(q,t)\,{\rm d}t. \tag{8}$$

In the Monte Carlo calculation, each trajectory is followed until decay. Thus, the total decay probability is unity, and no additional finite-time normalization is required.

The primary mass yield is then calculated as

$$Y_{\rm pre}(A) = \sum_q P_f(q) \sum_{i=1}^{2} \delta_{A_i(q),A}. \tag{9}$$

B. Total kinetic energy

The total kinetic energy is a property of the fragment pair as a whole rather than of either fragment individually. For a scission configuration defined at $R_m(q)$, the asymptotic TKE is estimated from the total energy associated with relative motion at this distance,

$$\mathrm{TKE}(q) = K_R\left(q, R_m(q)\right) + V_{\rm int}\left(q, R_m(q)\right), \tag{10}$$

where $K_R(q, R_m)$ is the radial kinetic energy of the relative motion. This contribution is not calculated explicitly in the present study. However, escape from the potential pocket requires sufficient energy to overcome the outer radial barrier: $K_R\left(q, R_m(q)\right) \geq V_B(q)$. As a near-threshold estimate, we take

$$K_R\left(q, R_m(q)\right) \simeq V_B(q) = V_{\rm int}\left(q, R_b(q)\right) - V_{\rm int}\left(q, R_m(q)\right). \tag{11}$$

Substitution into Eq. (10) yields

$$\mathrm{TKE}(q) \simeq V_{\rm int}\left(q, R_b(q)\right) = V_C\left(q, R_b(q)\right) + V_N\left(q, R_b(q)\right), \tag{12}$$

where $R_b(q)$ is the position of the outer barrier in the relative-distance coordinate for the pole–pole configuration.

The approximation in Eq. (12) corresponds to a trajectory that reaches the top of the radial barrier with negligible excess kinetic energy. As the fragments move beyond $R_b(q)$, their density overlap and the attractive nuclear interaction decrease rapidly. The remaining interfragment potential energy is converted predominantly into relative kinetic energy through Coulomb acceleration. Excess radial kinetic energy above the barrier and dissipative energy exchange during separation are neglected. For a configuration without an outer radial barrier, the same prescription reduces to $V_B(q) = 0$ and $\mathrm{TKE}(q) \simeq V_{\rm int}(q, R_m(q))$.

Using the decay probabilities $P_f(q)$ defined in Eq. (8), the average total kinetic energy is calculated as

$$\overline{\mathrm{TKE}} = \sum_q P_f(q)\,\mathrm{TKE}(q). \tag{13}$$

The average TKE associated with primary fragments of mass A is given by

$$\overline{\mathrm{TKE}}(A) = \frac{\sum_q P_f(q)\,\mathrm{TKE}(q) \sum_{i=1}^{2} \delta_{A_i(q),A}}{Y_{\rm pre}(A)}, \tag{14}$$

where $Y_{\rm pre}(A)$ is defined in Eq. (9). Because TKE characterizes the relative motion of the fragment pair, the same value $\mathrm{TKE}(q)$ is assigned to both complementary fragments produced from a given DNS configuration. Equation (14) refers to primary fragment masses. Comparison with post-neutron fragment masses therefore requires accounting for the mass changes caused by prompt neutron

CPC Accepted

emission.

C. Fragment deformation and excitation energy

The excitation energy of a primary fragment consists of an intrinsic component and the deformation energy stored in its nonequilibrium shape at scission:

$$E(Z,A,\beta^{\rm sc}) = E^{*}(Z,A) + E^{\rm def}(Z,A,\beta^{\rm sc}). \tag{15}$$

Here, $\beta^{\rm sc}$ denotes the fragment deformation at scission, which generally differs from its ground-state value, $\beta^{\rm gs}$. For each DNS configuration q, the available intrinsic excitation energy is shared between the two fragments according to the prescription of Refs. [6, 22]. The resulting value of $E^{*}(Z,A)$ therefore depends implicitly on the DNS configuration from which the fragment is formed.

The deformation energy is evaluated using the microscopic–macroscopic approach employed in the improved scission-point model [3, 4]:

$$E^{\rm def}(Z,A,\beta^{\rm sc}) = E^{\rm mac-mic}(Z,A,\beta^{\rm sc}) - E^{\rm mac-mic}(Z,A,\beta^{\rm gs}). \tag{16}$$

This microscopic–macroscopic description is used because it systematically provides deformation-dependent energies across the full range of fragments while explicitly accounting for the shell and pairing effects that determine their equilibrium shapes and resistance to deformation.

After scission, each fragment relaxes toward its equilibrium shape. The released deformation energy is converted into intrinsic excitation energy and becomes available for neutron and γ emission. Consequently, fragments formed with strongly nonequilibrium deformations generally acquire higher excitation energies and emit more neutrons. In contrast, fragments formed near shell-stabilized equilibrium shapes have lower deformation energies and, consequently, emit fewer neutrons on average.

Let $F(s,E)$ denote the probability that a fragment with initial excitation energy E emits s neutrons during de-excitation. This probability is calculated using the statistical de-excitation procedure described in Ref. [22]. The average number of neutrons emitted by fragment i belonging to the DNS configuration q is then

$$\bar{\nu}_i(q) = \sum_{s=0}^{s_{\max}} s\,F\left[s, E_i(q)\right], \qquad i = 1,2, \tag{17}$$

where $E_i(q) = E\left[Z_i(q), A_i(q), \beta_i^{\rm sc}(q)\right]$.

D. Angular momenta of the primary fragments

The angular motion of the DNS is treated quantum mechanically for each configuration q. The direction of the relative-distance vector $\boldsymbol{R} = (R_m, \theta_0, \phi_0)$ is specified by the angles $\Omega_0 = (\theta_0, \phi_0)$, whereas the orientations of the symmetry axes of the fragments are described by the angles $\Omega_i = (\phi_i, \theta_i, 0)$, $(i = 1,2)$. Here, $R_m(q)$ denotes the position of the minimum of the radial potential pocket introduced in Eq. (1), evaluated for the pole–pole orientation of the fragments. When solving the angular problem, this distance is held fixed, while the orientation dependence is included in the interaction potential.

To describe small-amplitude angular motion about the pole–pole configuration, we introduce the distortion angle ε_i, which measures the angular displacement of the symmetry axis of fragment i from its equilibrium pole–pole orientation. Its root-mean-square value in the lowest angular-vibrational state is denoted by $\varepsilon_{0i} = \sqrt{\langle \varepsilon_i^2 \rangle}$. In the harmonic limit, the angular vibration is characterized by the effective rotational inertia $\mathcal{J}_{b,i}$ and the frequency ω_i. The virial theorem yields the characteristic relation

$$\hbar I_{i,\rm rms} \simeq \mathcal{J}_{b,i}\omega_i\varepsilon_{0i}, \tag{18}$$

up to the usual numerical factor associated with the precise definition of the rms quantities. Equivalently, the same scaling follows from the angle–angular-momentum uncertainty relation. Thus, localization of the fragment axis within a narrower angular interval is accompanied by a broader angular-momentum distribution. The dependence of ε_{0i} on fragment deformation arises through the deformation dependence of the angular restoring interaction, vibrational frequency, and moment of inertia, as discussed in Ref. [6].

The assumed intrinsic axial symmetry of each fragment must be distinguished from the symmetry of the complete DNS configuration. The independent orientation coordinates Ω_0, Ω_1, and Ω_2 do not restrict the composite system to an axially symmetric shape. Axial symmetry is recovered only for special aligned configurations, such as the pole–pole minimum, whereas angular vibrations about this minimum generally correspond to nonaxial instantaneous DNS configurations. Thus, the collective angular Hamiltonian explicitly includes dynamical breaking of the axial symmetry of the composite system, although intrinsic nonaxial deformations of the individual fragments are not included.

The direct connection between angular vibrations and nonaxiality was demonstrated in a related DNS description of heavy nuclear molecules. In that description, pole–pole angular vibrations were shown to generate nonaxial configurations and a nonzero projection K of the total angular momentum onto the intrinsic molecular axis [23]. Here, the collective projection K of the complete system should not be confused with the intrinsic fragment projections K_i, which are set to zero in the present calculation.

CPC Accepted

For a fixed DNS configuration q, the collective angular Hamiltonian is written as

$$\hat{H}_{\rm ang}(q) = \frac{\hbar^2 \hat{I}_0^2}{2\mu(q)R_m^2(q)} + \sum_{i=1}^{2} \frac{\hbar^2 \hat{I}_i^2}{2\mathcal{J}_{\perp i}(q)} + V_{\rm ang}(q;\Omega_0,\Omega_1,\Omega_2), \tag{19}$$

where $\hat{I}_0$ is the relative angular-momentum operator, $\hat{I}_1$ and $\hat{I}_2$ are the angular-momentum operators of the fragments, and $\mu(q)$ is their reduced mass. The operators $\hat{I}_j$ are dimensionless; thus, the calculated angular momenta are expressed in units of $\hbar$.

The fragments are assumed to be axially symmetric, with $K_i = 0$. Their rotational kinetic energies therefore depend only on the moments of inertia about axes perpendicular to their symmetry axes, $\mathcal{J}_{\perp i}(q)$. These moments of inertia are obtained by smooth interpolation between the corresponding rigid-body and irrotational-flow limits, denoted by $\mathcal{J}_{\perp i}^{\rm rig}$ and $\mathcal{J}_{\perp i}^{\rm irr}$, respectively:

$$\mathcal{J}_{\perp i}(q) = \mathcal{J}_{\perp i}^{\rm irr}(q) + g\left[\beta_i(q)\right]\left[\mathcal{J}_{\perp i}^{\rm rig}(q) - \mathcal{J}_{\perp i}^{\rm irr}(q)\right], \tag{20}$$

with the exponential saturation factor

$$g(\beta) = 1 - \exp\left[-\ln 2\left(\frac{\beta}{\beta_{1/2}}\right)^2\right], \qquad \beta_{1/2} = 0.25. \tag{21}$$

Thus, $g(0) = 0$, $g(\beta_{1/2}) = 1/2$, and $g(\beta) \to 1$ asymptotically at large deformation. This interpolation ensures the appropriate behavior of the collective rotational degree of freedom as the fragment approaches sphericity. For a spherical fragment, the orientation of a symmetry axis is physically redundant, and rotational excitations associated with this degree of freedom should not contribute to the low-energy spectrum. Since the rotational excitation energies scale approximately as $\hbar^2 I(I+1)/(2\mathcal{J}_\perp)$, retaining a finite rigid-body moment of inertia in the spherical limit would yield spurious finite-energy rotational states. In contrast, the irrotational-flow moment of inertia tends to zero as $\beta \to 0$, causing the energies of the rotational $I > 0$ states to diverge and leaving only the $I = 0$ component in the low-energy angular wave function. At finite deformation, the moment of inertia is allowed to evolve smoothly toward the rigid-body limit.

The parameter $\beta_{1/2}$ controls the deformation scale of this crossover. We use $\beta_{1/2} = 0.25$. A calculation with $\beta_{1/2} = 0.35$ yields a nearly identical mass dependence of the fragment angular momenta, demonstrating that the results are insensitive to the precise choice of the crossover parameter.

The angular potential $V_{\rm ang}(q;\Omega_0,\Omega_1,\Omega_2)$ is obtained from the orientation-dependent nuclear and Coulomb interactions between the fragments at $R_m(q)$. For deformed fragments, the interaction energy generally has minima at preferred mutual orientations. Deviations from these orientations increase the interaction energy and produce restoring torques, giving rise to angular vibrations and nonzero fragment angular momenta. The strength of the restoring force depends strongly on the fragment deformations, providing a direct connection between the scission shapes and the angular momenta of the primary fragments.

In the spherical limit, the interaction does not depend on the direction assigned to the symmetry axis of the corresponding fragment. Rotation of this axis therefore produces neither a change in the interaction energy nor a restoring torque. Consequently, the angular momentum generated by this mechanism approaches zero for nearly spherical fragments, essentially independently of the moment of inertia used in their rotational kinetic energy. This suppression contributes substantially to the sawtooth mass dependence of the fragment angular momenta.

For spontaneous fission from the 0^+ ground state of ^{252}Cf, the eigenfunctions of Eq. (19) are expanded in angular-momentum states coupled to total angular momentum zero:

$$\Psi_x^{\rm ang}(q) = \sum_{I_0 I_1 I_2} a_{I_0 I_1 I_2}^{(x)}(q)\left|[I_0 \otimes [I_1 \otimes I_2]_{I_0}]_{00}\right\rangle, \tag{22}$$

where x labels an eigenstate of the angular Hamiltonian. The probability of finding the angular-momentum combination (I_0, I_1, I_2) in this state is

$$\mathcal{P}_x(q;I_0,I_1,I_2) = \left|a_{I_0 I_1 I_2}^{(x)}(q)\right|^2. \tag{23}$$

We characterize the angular momentum of subsystem $j = 0,1,2$ in state x by its root-mean-square magnitude, $I_{j,\rm rms}^{(x)} = \sqrt{\langle \hat{I}_j^2 \rangle_x}$, expressed in units of $\hbar$. Using the probabilities defined in Eq. (23), we calculate this quantity as

$$I_{j,\rm rms}^{(x)}(q) = \left[\sum_{I_0 I_1 I_2} I_j(I_j+1)\mathcal{P}_x(q;I_0,I_1,I_2)\right]^{1/2}. \tag{24}$$

Thus, $I_{j,\rm rms}^{(x)}$ denotes the rms magnitude of the angular-momentum vector.

Using the angular-state occupation probabilities $w_x(q)$ introduced in Eq. (7), the corresponding ensemble-averaged angular-momentum magnitude of subsystem j for a given DNS configuration is expressed as

$$\bar{I}_j(q) = \sum_x w_x(q) I_{j,\rm rms}^{(x)}(q), \qquad j = 0,1,2. \tag{25}$$

CPC Accepted

In the low-temperature limit, where the lowest angular-vibrational state dominates, this expression reduces to $\bar{I}_j(q) \simeq I^{(0)}_{j,\mathrm{rms}}(q)$. The angular momenta of the two primary fragments are obtained by setting $j = 1$ and $j = 2$, respectively.

E. Mass-dependent fragment spin and post-neutron observables

Using the primary mass yield defined in Eq. (9), we calculate the average angular momentum of primary fragments with mass A as

$$\bar{I}_{\mathrm{pre}}(A) = \frac{\sum_q P_f(q) \sum_{i=1}^{2} \bar{I}_i(q) \delta_{A_i(q),A}}{Y_{\mathrm{pre}}(A)}. \tag{26}$$

Here, $\bar{I}_i(q)$ is the average angular momentum of fragment i in configuration q, as defined in Eq. (25), and is expressed in units of $\hbar$.

Equation (26) refers to the pre-neutron fragment mass. Prompt-neutron emission changes the fragment mass while leaving its charge unchanged. Using the neutron-emission probabilities $F[s, E_i(q)]$, the post-neutron yield of a given isotope (Z,A) is calculated as

$$Y_{\mathrm{post}}(Z,A) = \sum_q P_f(q) \sum_{i=1}^{2} \sum_{s=0}^{s_{\max}} F[s, E_i(q)] \delta_{Z_i(q),Z} \delta_{A_i(q)-s,A}. \tag{27}$$

The corresponding mass yield is obtained by summing over the fragment charges: $Y_{\mathrm{post}}(A) = \sum_Z Y_{\mathrm{post}}(Z,A)$.

Prompt-neutron emission can also modify the fragment angular momentum. To estimate schematically the angular momentum carried away by the emitted neutrons, we assume s-wave neutron emission. This assumption is motivated by the centrifugal suppression of high-ℓ neutron emission. For $\ell = 0$, the emitted neutron carries total angular momentum $j = 1/2$. We therefore approximate the change in the magnitude of the fragment angular momentum as $1/2$ per emitted neutron. Within this schematic prescription, after the emission of s neutrons,

$$\bar{I}_i^{(s)}(q) = \max\left[0, \bar{I}_i(q) - \frac{s}{2}\right]. \tag{28}$$

However, microscopic decay calculations show that neutron and γ emission can reshape fragment-spin distributions in a more complex manner [24].

The average angular momentum of post-neutron fragments of isotope (Z,A) is then

$$\bar{I}_{\mathrm{post}}(Z,A) = \frac{\sum_q P_f(q) \sum_{i=1}^{2} \sum_{s=0}^{s_{\max}} \bar{I}_i^{(s)}(q) F[s, E_i(q)] \delta_{Z_i(q),Z} \delta_{A_i(q)-s,A}}{Y_{\mathrm{post}}(Z,A)}. \tag{29}$$

The corresponding charge-averaged angular momentum for a given post-neutron mass A is calculated as the yield-weighted average of the isotope-resolved values,

$$\bar{I}_{\mathrm{post}}(A) = \frac{\sum_Z Y_{\mathrm{post}}(Z,A) \bar{I}_{\mathrm{post}}(Z,A)}{\sum_Z Y_{\mathrm{post}}(Z,A)}. \tag{30}$$

The two observables serve distinct purposes in the following analysis. The isotope-resolved quantity $\bar{I}_{\mathrm{post}}(Z,A)$ is used for isotope-by-isotope comparisons with experimentally identified fragments, whereas $\bar{I}_{\mathrm{post}}(A)$ is used to test whether the global mass dependence persists after averaging over the fragment charge distribution.

As a complementary test of the calculated neutron emission, we also consider the average total number of neutrons emitted in events within a TKE bin centered at $\mathcal{T}$:

$$\bar{\nu}(\mathcal{T}) = \frac{\sum_q P_f(q) \left[\bar{\nu}_1(q) + \bar{\nu}_2(q)\right] \chi_{\mathcal{T}}\left[\mathrm{TKE}(q)\right]}{\sum_q P_f(q) \chi_{\mathcal{T}}\left[\mathrm{TKE}(q)\right]}, \tag{31}$$

where $\chi_{\mathcal{T}}[\mathrm{TKE}(q)]$ equals unity when $\mathrm{TKE}(q)$ lies within the selected bin and vanishes otherwise. For each configuration q, the quantity $\bar{\nu}_1(q) + \bar{\nu}_2(q)$ is the average total number of neutrons emitted by the complementary fragments.

The angular-momentum observables analyzed below are the isotope-resolved $\bar{I}_{\mathrm{post}}(Z,A)$ and the charge-averaged $\bar{I}_{\mathrm{post}}(A)$. The neutron-emission probabilities affect both quantities through migration from primary to post-neutron masses and through the schematic spin correction in Eq. (28). In addition, $\bar{\nu}(\mathcal{T})$ tests the relationship between fragment excitation and the compactness of the scission configuration. No comparison of neutron multiplicity as a function of fragment mass is required for these purposes.

III. RESULTS AND DISCUSSION

A. Initial DNS ensemble and evolution toward scission

After penetrating the fission barrier, the fissioning nucleus becomes strongly elongated and develops a pronounced two-center structure. At this stage, it is represented by a superposition of touching DNS configurations

CPC Accepted

rather than a single binary partition. The initial ensemble is restricted to configurations that satisfy

$$\left|Q_{20}(q)-Q_{20}^{(3:1)}\right| \le 0.1\,Q_{20}^{(3:1)}, \tag{32}$$

where $Q_{20}^{(3:1)}$ is the quadrupole moment of an equivalent ellipsoid with a major-to-minor semi-axis ratio of $3:1$. Such an elongation is characteristic of the hyperdeformed regime, in which strongly elongated one-body shapes acquire properties similar to those of touching cluster configurations [25−28].

The 10% interval in Eq. (32) should not be interpreted as a sharp physical boundary. It defines a finite region around the chosen elongation and allows different mass, charge, and deformation partitions to contribute to the initial DNS superposition. Thus, no particular fragment partition is singled out. The choice of the initial DNS ensemble follows Ref. [9], in which the parameters defining the initial configuration for ^{252}Cf were determined through a simultaneous description of the main fission observables, including the fragment-mass, TKE, and neutron-emission distributions. The same initial ensemble is used here without further adjustment to calculate the angular-momentum observables and their correlations. Using the same assumptions and parameter set, Refs. [9, 22] described the fragment-mass and TKE distributions, neutron multiplicities, and the dependence of neutron multiplicity on TKE.

The set of configurations satisfying Eq. (32) is denoted by $\mathcal{S}_0$. The initial weight of each configuration is calculated according to the microscopic level density of the corresponding DNS:

$$P_0(q)=\begin{cases}\dfrac{\rho\left[E^*(q),q\right]}{\sum\limits_{q'\in\mathcal{S}_0}\rho\left[E^*(q'),q'\right]}, & q\in\mathcal{S}_0,\\ 0, & q\notin\mathcal{S}_0.\end{cases} \tag{33}$$

Consequently, configurations with higher densities of accessible states are assigned higher initial probabilities.

The subsequent evolution proceeds through transitions between neighboring configurations in mass, charge, and fragment-deformation space. The transition rates are determined from the microscopic level densities of the initial and final DNS configurations. For a given DNS, the intrinsic level density is obtained by folding the level densities of its two constituent fragments,

$$\rho_{\rm in}(E^*,q)=\int_0^{E^*}\rho_1(\varepsilon,q)\rho_2(E^*-\varepsilon,q)\,{\rm d}\varepsilon, \tag{34}$$

and the angular states are explicitly included through

$$\rho(E^*,q)=\sum_x\rho_{\rm in}\left(E^*-E_x^{\rm ang}(q),q\right). \tag{35}$$

The fragment level densities are calculated using the actual fragment masses, charges, deformations, and excitation energies [29]. Consequently, shell and pairing effects enter the transition rates explicitly. Shell gaps and pairing correlations suppress the density of accessible states at low excitation energies, whereas their gradual damping with increasing excitation energy opens additional transition channels. The resulting scission distribution is therefore governed not only by the potential-energy landscape but also by the deformation- and excitation-dependent microscopic phase space available during the DNS evolution.

B. Fragment deformations and neutron emission

Figure 1 compares the calculated mass dependence of the prompt-neutron multiplicity with the experimental data from Ref. [1] and presents representative joint deformation distributions for three populated fragment pairs. The pairs were selected so that their six constituent fragment masses span the region over which the sawtooth dependence of the prompt-neutron multiplicity is measured, including the shell-associated minimum near $A\simeq 132$ and the regions on both sides. These pairs also exhibit qualitatively different scission-deformation patterns, as discussed below.

In the lower panels, β_L and β_H denote the deformations of the light and heavy fragments at scission, respectively. For visualization, each joint deformation distribution is divided by its maximum value for the indicated mass–charge partition. The common color scale therefore represents $P(\beta_L,\beta_H)/P_{\rm max}$ and facilitates comparison of the locations and spreads of the distributions. It should not be used to compare their absolute probabilities.

The connection to the neutron multiplicities shown in the upper panel arises from the deformation energy stored in the nonequilibrium fragment shapes. During post-scission relaxation, this energy is converted into intrinsic excitation and becomes available for neutron emission. Consequently, a joint distribution in the (β_L,β_H) plane corresponds to a distribution of deformation energies and neutron-emission probabilities. The calculated multiplicity for a given fragment is therefore an average over all scission configurations contributing to that fragment, rather than the result of a single deformation.

This relationship is particularly clear for the ^{120}Cd + ^{132}Sn pair. The deformation distribution of the shell-stabilized ^{132}Sn heavy fragment is concentrated at small values of β_H, corresponding to relatively low deformation energies. This produces the pronounced reduction in the calculated neutron multiplicity near $A\simeq 132$. Its complementary ^{120}Cd light fragment populates appre-

CPC Accepted

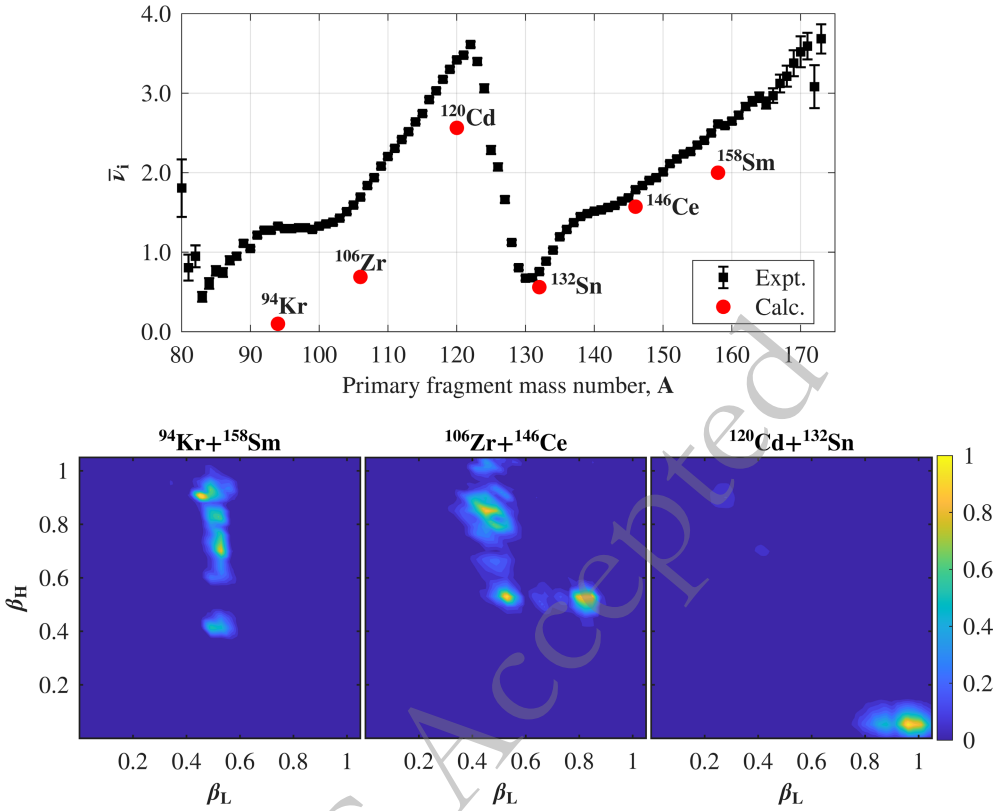


Fig. 1. (color online) Upper panel: average prompt-neutron multiplicity as a function of primary fragment mass. Black squares show the experimental values from Ref. [1], while red circles indicate the calculated values for the selected fragments. Lower panels: calculated normalized joint distributions in the (β_L,β_H) plane for the representative fragment pairs ^{94}Kr + ^{158}Sm, ^{106}Zr + ^{146}Ce, and ^{120}Cd + ^{132}Sn. Here, β_L and β_H denote the scission deformations of the light and heavy fragments, respectively. The common color bar indicates the values of each distribution normalized to its own maximum, $P(\beta_L,\beta_H)/P_{\max}$.

CPC Accepted

ciably larger values of β_L and therefore releases more deformation energy during relaxation, resulting in a larger neutron multiplicity. The finite width of the ^{132}Sn distribution shows, however, that this fragment is not restricted to an exactly spherical scission shape.

For the ^{106}Zr + ^{146}Ce pair, both fragments populate strongly deformed configurations. The corresponding higher deformation energies increase the excitation available for neutron emission and lead to larger calculated multiplicities than those in the shell-stabilized $A \simeq 132$ region. The ^{94}Kr + ^{158}Sm pair exhibits broader joint deformation distributions. The neutron multiplicities for this pair consequently include contributions from a wider range of scission shapes and deformation energies, demonstrating that a single mass–charge partition cannot, in general, be associated with a unique scission deformation.

These examples establish the connection between the mass dependence of the neutron multiplicity and the underlying fragment-deformation distributions. The neutron multiplicity is not determined by deformation alone, because the partition of the intrinsic excitation energy and the neutron separation energies also contribute. Nevertheless, the shell-dependent deformation energy provides the direct link between the scission configurations in the lower panels and the variation in $\bar{\nu}(A)$ in the upper panel. The same deformation distributions also determine the orientation-dependent interaction and therefore enter the calculation of the fragment angular momenta discussed below.

C. Representative angular-momentum distributions

Figure 2 illustrates the relationship between the localization of the fragment orientation and its angular-momentum distribution for two representative rms distortion angles, $\varepsilon_{01} = 0.1$ and 0.3. As defined above, ε_{01} characterizes the zero-point angular oscillation of the fragment symmetry axis about the pole–pole configuration. The smaller value therefore corresponds to stronger localization in the angular coordinate. For small-amplitude oscillations, the virial relation in Eq. (18), or equivalently the angle–angular-momentum uncertainty relation, implies that stronger angular localization is accompanied by a broader angular-momentum distribution. Accordingly, the distribution for $\varepsilon_{01} = 0.1$ extends to substantially larger values of I, whereas the distribution for $\varepsilon_{01} = 0.3$ is concentrated at smaller angular momenta.

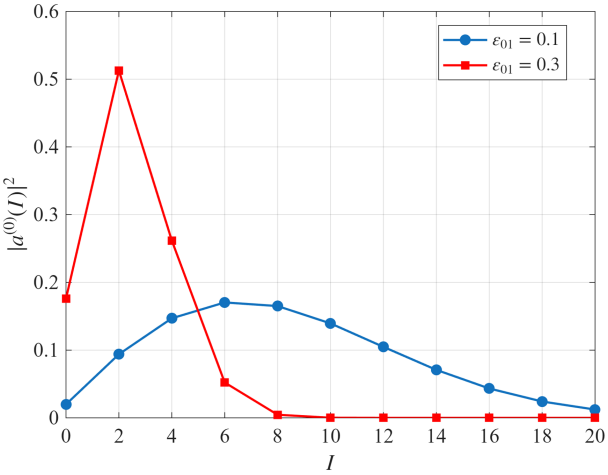


Fig. 2. (color online) Representative angular-momentum probabilities $|a^{(0)}(I)|^2$ in the lowest angular-vibrational state for rms distortion angles $\varepsilon_{01} = 0.1$ (blue circles) and $\varepsilon_{01} = 0.3$ (red squares). Here, ε_{01} measures the rms angular displacement of the fragment symmetry axis from the pole–pole orientation. The smaller distortion angle corresponds to stronger localization in the angular coordinate and, consequently, a broader angular-momentum distribution.

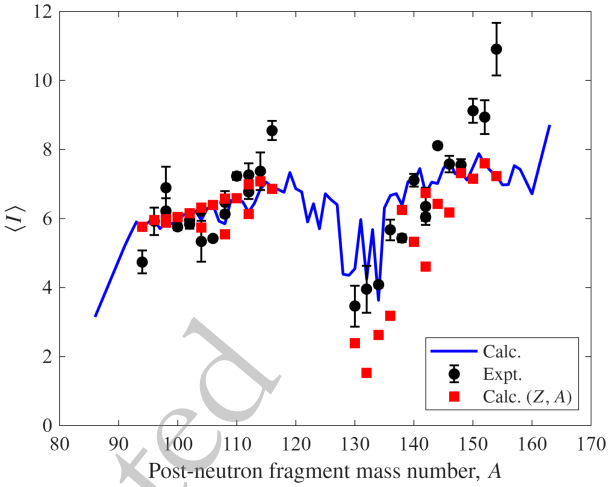


Fig. 3. (color online) Average angular momentum of post-neutron fission fragments in the spontaneous fission of ^{252}Cf. Black circles with error bars denote the isotope-resolved experimental values of Wilson et al. [7]. Red squares denote the corresponding isotope-resolved DNS calculations $\bar{I}_{\rm post}(Z,A)$ for the same nuclei, enabling isotope-by-isotope comparison with the experimental values. The solid blue curve shows the charge-averaged quantity $\bar{I}_{\rm post}(A)$, obtained by averaging over all charge partitions contributing to each final fragment mass.

The distortion angle is not itself a quadrupole-deformation parameter. Its connection to fragment deformation is indirect: deformation modifies the angular restoring interaction, the vibrational frequency, and the moment of inertia, thereby changing ε_{0i} and the resulting angular-momentum distribution. As shown in Ref. [6], increasing fragment deformation generally strengthens angular localization and increases the characteristic fragment angular momentum. The distributions in Fig. 2 therefore illustrate the mechanism connecting scission deformation to fragment spin, rather than representing universal distributions associated with fixed values of β.

D. Mass dependence of fragment angular momentum

Figure 3 summarizes the calculated mass dependence of the post-neutron fragment angular momenta. Two related theoretical quantities are shown. The red symbols represent the isotope-resolved values $\bar{I}_{\rm post}(Z,A)$ calculated for the same nuclei for which experimental angular momenta were extracted by Wilson et al. [7]. These values therefore allow an isotope-by-isotope comparison with the experimental data. The numerical values are also listed in Table 1. No calculated value is given for ^{102}Mo because this isotope is not populated in the calculated post-neutron fragment distribution. Its production probability is therefore zero, and its average angular momentum is undefined. The isotope-resolved calculation reproduces the experimentally observed mass dependence of the fragment angular momentum, including the strong suppression near the $Z = 50$, $N = 82$ shell region, although deviations remain for individual nuclei.

The calculated angular momenta tend to underestimate the experimental values for several Sn–Te nuclei near the shell-associated minimum. In this region, the calculated values are especially sensitive to the distribution of small scission deformations and to the conversion from primary to post-neutron fragment observables. This sensitivity is closely related to the angular-momentum-generation mechanism adopted here. In the present treatment, the fragment angular momenta arise from relative angular vibrations in the DNS, described through the coupling of the fragments' collective rotational states to their relative orbital motion. This mechanism is particularly appropriate for deformed fragments, for which rotational excitations are among the lowest-energy collective modes, and provides a natural description of the overall mass-dependent trend. For spherical and nearly spherical fragments, dynamical shape vibrations and intrinsic quasiparticle excitations may also contribute as rotational collectivity weakens, possibly accounting for part of the local discrepancy near ^{132}Sn. In addition, the experimental angular momenta are inferred from the feeding of low-lying states, whereas direct feeding of the 0^+ ground state must be estimated by extrapolation. Given the sparse low-lying level schemes near the closed shells, underestimating this contribution could bias the inferred average angular momentum upward [7, 24].

The solid blue curve in Fig. 3 shows the charge-averaged quantity $\bar{I}_{\rm post}(A)$ defined in Eq. (30). Notably, the pronounced sawtooth dependence is preserved under this

CPC Accepted

Table 1. Calculated and experimental post-neutron-emission fragment angular momenta in the spontaneous fission of ^{252}Cf. Experimental values are taken from Ref. [7].

Nucleus	DNS	Experiment	Nucleus	DNS	Experiment
^{94}Sr	5.74	4.74 ± 0.33	^{130}Sn	2.37	3.46 ± 0.59
^{96}Sr	5.96	5.92 ± 0.40	^{132}Sn	1.53	3.95 ± 0.68
^{98}Sr	5.89	6.89 ± 0.61	^{134}Te	2.63	4.08 ± 0.08
^{98}Zr	5.94	6.22 ± 0.37	^{136}Te	3.18	5.67 ± 0.30
^{100}Zr	6.04	5.76 ± 0.10	^{138}Xe	6.25	5.43 ± 0.11
^{102}Zr	6.15	5.84 ± 0.13	^{140}Xe	5.31	7.11 ± 0.19
^{104}Zr	5.73	5.34 ± 0.59	^{142}Xe	4.62	6.35 ± 0.54
^{102}Mo	–	5.96 ± 0.25	^{142}Ba	6.74	6.04 ± 0.10
^{104}Mo	6.30	6.22 ± 0.07	^{144}Ba	6.43	8.11 ± 0.09
^{106}Mo	6.40	5.42 ± 0.07	^{146}Ba	6.18	7.58 ± 0.24
^{108}Mo	5.54	6.13 ± 0.09	^{148}Ce	7.31	7.56 ± 0.16
^{108}Ru	6.58	6.47 ± 0.32	^{150}Ce	7.15	9.12 ± 0.35
^{110}Ru	6.59	7.23 ± 0.11	^{152}Nd	7.60	8.94 ± 0.49
^{112}Ru	6.14	6.77 ± 0.20	^{154}Nd	7.22	10.91 ± 0.76
^{112}Pd	6.97	7.26 ± 0.34			
^{114}Pd	7.07	7.37 ± 0.54			
^{116}Pd	6.86	8.55 ± 0.28			

CPC Accepted

charge averaging. In particular, the minimum around $A \simeq 132$ remains clearly visible. Thus, the calculated sawtooth structure is not a consequence of the particular sequence of isotopes selected experimentally, but is a robust property of the mass-dependent ensemble of scission configurations.

Within the present model, this robustness reflects the systematic variation of fragment deformation with mass. Near $A \simeq 132$, the populated configurations contain fragments in the shell-stabilized ^{132}Sn region with small deformations. Their relatively weak orientation-dependent interaction generates only a small restoring torque and hence relatively small angular momenta. Away from this region, larger scission deformations strengthen the angular restoring interaction and increase the generated spin.

An important limitation of the present calculation is its restriction to reflection-symmetric quadrupole-deformed fragments. Microscopic studies show that heavy fragments in the Ba–Ce region can acquire substantial octupole deformation and that octupole shell effects influence the preferred fission configurations [30]. Within a collective angular Hamiltonian, octupole deformation can also increase the generated fragment angular momentum [19]. Its inclusion would modify both the scission geometry and the orientation-dependent interaction and could therefore affect the quantitative description of heavy-fragment angular momenta. It may also modify TKE by changing the scission compactness [9]. These effects are left for a future extension of the present model.

Neutron emission affects both isotope-resolved and charge-averaged post-neutron observables through migration between mass bins and the angular momentum carried away during de-excitation. Together with the distribution of scission deformations, these effects can generate small-scale structures in the calculated results. Given the schematic *s*-wave prescription used to estimate the angular momentum carried away by prompt neutrons, such local structures should not be overinterpreted. This prescription primarily affects the quantitative conversion from primary to post-neutron angular momenta, whereas neutron-induced migration between fragment-mass bins is treated explicitly through the calculated evaporation probabilities. The robust result emphasized here is the global sawtooth pattern and its persistence under charge averaging.

E. Average neutron emission versus TKE

Figure 4 shows the average total number of neutrons emitted by the two complementary fragments as a function of TKE. The calculation reproduces the experimentally observed anticorrelation: fission events with higher TKE are accompanied, on average, by fewer emitted neutrons [1, 2]. The calculated absolute neutron multiplicities agree reasonably well with the experimental values over the main TKE range. In particular, the observed decrease in neutron multiplicity with increasing TKE is well reproduced.

In the present model, this result should not be inter-

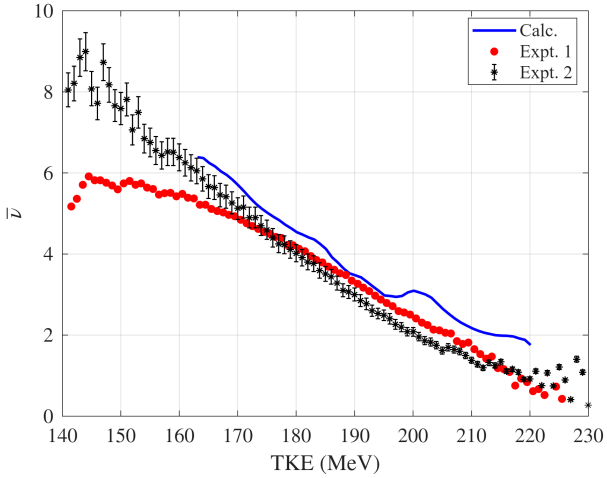


Fig. 4. (color online) Average total number of prompt neutrons $\bar{\nu}$ emitted by the two complementary fragments as a function of TKE. The solid blue curve shows the DNS calculation; the red circles and black asterisks represent the experimental results from Ref. [1] (Expt. 1) and Ref. [33] (Expt. 2), respectively.

preted solely in terms of a simple partition of the available energy between relative motion and fragment excitation. TKE is strongly influenced by the fragment deformations near scission. These deformations control the compactness of the scission configuration, the distance between the fragment charge centers, and, consequently, the Coulomb repulsion, which provides the dominant contribution to the final TKE. The strong sensitivity of TKE to fragment shapes at scission has also been demonstrated in dynamical calculations [31].

These same fragment deformations also determine the deformation energy released during post-scission relaxation. More elongated scission configurations generally have a greater distance between the charge centers and hence a smaller Coulomb contribution to TKE, while their larger deformation energies provide more energy for neutron emission. More compact configurations exhibit the opposite tendency. The calculated anticorrelation between $\bar{\nu}$ and TKE therefore reflects the dependence of both observables on fragment deformation at scission. This result emphasizes the role of the scission configuration and shows that the observed neutron–TKE dependence cannot be understood solely in terms of the excitation energy available to the fragments.

An important feature of this result is that no additional TKE-dependent assumption is introduced in the neutron-emission calculation. The fragment populations, deformations, TKE values, and neutron-emission probabilities are calculated simultaneously for the same ensemble of DNS configurations. The reproduction of the observed anticorrelation thus provides an additional nontrivial consistency check of the scission configurations used to explain the mass dependence of the fragment angular momentum.

Energy conservation naturally contributes to the anticorrelation because converting more of the available energy into relative motion generally leaves less energy for fragment de-excitation. However, this argument alone is insufficient to determine the observed trend. The plotted average includes configurations with different mass and charge partitions, Q values, scission compactness, intrinsic excitations, deformation energies, neutron separation energies, and microscopic level densities. Calculations that distinguish between intrinsic and distortion energies likewise show that the neutron–TKE correlation cannot be reduced to a single energy-partition rule [32].

The residual discrepancies at the lowest and highest TKE values are not central to the present analysis. Events in these regions have low probabilities, making both experimental and theoretical results less reliable. Moreover, as discussed in Ref. [9], the omission of fragment octupole deformations can lead to an overestimation of TKE. The main significance of Fig. 4 is therefore the reproduction of the overall anticorrelation without imposing an additional correlation between the two observables.

IV. CONCLUSIONS

The mass dependence of fission-fragment angular momenta in the spontaneous fission of ^{252}Cf has been studied within the DNS model. The calculated angular momenta reproduce the observed sawtooth trend, including the pronounced suppression near $A \simeq 132$. This structure persists after averaging over all charge partitions contributing to a given fragment mass, demonstrating that it is a robust property of the calculated scission ensemble rather than a consequence of the particular isotope sequence selected experimentally.

Within the present model, the sawtooth behavior arises primarily from shell-dependent fragment deformations at scission. Small deformations in the vicinity of the ^{132}Sn shell region lead to a weaker orientation-dependent interaction and smaller generated angular momenta, whereas larger deformations away from this region produce larger angular momenta. Reproducing the observed anticorrelation between $\bar{\nu}$ and TKE using the same ensemble of DNS configurations provides an additional consistency check on the calculated scission configurations and further supports this interpretation of the fragment angular-momentum systematics.

CPC Accepted

References

[1] A. Göök, F.-J. Hambsch, and M. Vidali, Phys. Rev. C **90**, 064611 (2014)
[2] C. Budtz-Jørgensen and H.-H. Knitter, Nucl. Phys. A **490**, 307 (1988)
[3] A. V. Andreev, G. G. Adamian, N. V. Antonenko, S. P. Ivanova, and W. Scheid, Eur. Phys. J. A **22**, 51 (2004)
[4] A. V. Andreev, G. G. Adamian, N. V. Antonenko, and S. P. Ivanova, Eur. Phys. J. A **26**, 327 (2005)
[5] H. Paşca, A. V. Andreev, G. G. Adamian, and N. V. Antonenko, Phys. Rev. C **104**, 014604 (2021)
[6] T. M. Shneidman, A. Rahmatinejad, G. G. Adamian, and N. V. Antonenko, Phys. Rev. C **111**, 064621 (2025)
[7] J. N. Wilson *et al*., Nature **590**, 566 (2021)
[8] N. P. Giha, S. Marin, I. A. Tolstukhin, M. B. Oberling, R. A. Knaack, C. Mueller-Gatermann, A. Korichi, K. Bhatt, M. P. Carpenter, C. Fougères, V. Karayonchev, B. P. Kay, T. Lauritsen, D. Seweryniak, N. Watwood, D. L. Duke, S. Mosby, K. B. Montoya, D. S. Connolly, W. Loveland, I. E. Hernandez, S. D. Clarke, S. A. Pozzi, and F. Tovesson, Phys. Rev. C **111**, 014605 (2025)
[9] A. Rahmatinejad, T. M. Shneidman, G. G. Adamian, and N. V. Antonenko, Phys. Rev. C **112**, 044610 (2025)
[10] J. Randrup and R. Vogt, Phys. Rev. Lett. **127**, 062502 (2021)
[11] T. Døssing, S. Åberg, M. Albertsson, B. G. Carlsson, and J. Randrup, Phys. Rev. C **109**, 034615 (2024)
[12] J. Randrup, P. Nadtochy, C. Schmitt, and K. Mazurek, Phys. Rev. C **113**, 044605 (2026)
[13] G. F. Bertsch, T. Kawano, and L. M. Robledo, Phys. Rev. C **99**, 034603 (2019)
[14] A. Bulgac, I. Abdurrahman, S. Jin, K. Godbey, N. Schunck, and I. Stetcu, Phys. Rev. Lett. **126**, 142502 (2021)
[15] A. Bulgac, I. Abdurrahman, K. Godbey, and I. Stetcu, Phys. Rev. Lett. **128**, 022501 (2022)
[16] P. Marević, N. Schunck, J. Randrup, and R. Vogt, Phys. Rev. C **104**, L021601 (2021)
[17] P. Marević, N. Schunck, and M. Verrière, Phys. Rev. C **113**, 014612 (2026)
[18] G. Scamps, I. Abdurrahman, M. Kafker, A. Bulgac, and I. Stetcu, Phys. Rev. C **108**, L061602 (2023)
[19] G. Scamps and G. F. Bertsch, Phys. Rev. C **108**, 034616 (2023)
[20] G. Scamps, A. Guilleux, D. Regnier, and A. Bernard, Uncertainty principle and angular momentum generation in microscopic fission models (2026), revised July 2026, arXiv: 2512.02207 [nucl-th].
[21] B. Li, D. D. Zhang, D. Vretenar, T. Nikšić, P. W. Zhao, and J. Meng, Phys. Rev. Lett. **136**, 252502 (2026)
[22] A. Rahmatinejad, A. V. Andreev, A. N. Bezbakh, A. V. Isaev, R. S. Mukhin, and T. M. Shneidman, Int. J. Mod. Phys. E **33**, 2441018 (2024)
[23] T. M. Shneidman and R. G. Nazmitdinov, J. Phys. A: Math. Theor. **59**, 215203 (2026), arXiv: 2601.16600[nucl-th]
[24] I. Stetcu, A. E. Lovell, P. Talou, T. Kawano, S. Marin, S. A. Pozzi, and A. Bulgac, Phys. Rev. Lett. **127**, 222502 (2021)
[25] W. Nazarewicz and J. Dobaczewski, Phys. Rev. Lett. **68**, 154 (1992)
[26] S. Ćwiok, W. Nazarewicz, J. X. Saladin, W. P lociennik, and A. Johnson, Phys. Lett. B **322**, 304 (1994)
[27] S. Åberg and L.-O. Jönsson, Z. Phys. A **349**, 205 (1994)
[28] T. M. Shneidman, G. G. Adamian, N. V. Antonenko, S. P. Ivanova, and W. Scheid, Nucl. Phys. A **671**, 119 (2000)
[29] A. N. Bezbakh, T. M. Shneidman, G. G. Adamian, N. V. Antonenko, and S.-G. Zhou, Eur. Phys. J. A **52**, 353 (2016)
[30] G. Scamps and C. Simenel, Nature **564**, 382 (2018)
[31] K. Shimada, C. Ishizuka, F. A. Ivanyuk, and S. Chiba, Phys. Rev. C **104**, 054609 (2021)
[32] M. Albertsson, B. G. Carlsson, T. Døssing, P. Møller, J. Randrup, and S. Åberg, Phys. Rev. C **103**, 014609 (2021)
[33] S. Zeynalov, F.-J. Hambsch, and S. Oberstedt, J. Korean Phys. Soc. **59**, 1396 (2011)

CPC Accepted